A multiregion operator-splitting CFD approach for coupling microkinetic modeling with internal porous transport in heterogeneous catalytic reactors

Tiziano Maffei [a,1], *Giancarlo Gentile* [b,1], *Stefano Rebughini* [a,1], *Mauro Bracconi* [a], *Filippo Manelli* [a,b], *Stefan Lipp* [c], *Alberto Cuoci* [b], *Matteo Maestri* [a,*]

[a] Laboratory of Catalysis and Catalytic Processes – Dipartimento di Energia, Politecnico di Milano, Piazza Leonardo da Vinci 32, 20133 Milano, Italy
[b] Dipartimento di Chimica, Materiali e Ingegneria Chimica, Politecnico di Milano, Piazza Leonardo da Vinci 32, 20133 Milano, Italy
[c] BASF SE, GCP/RC – L540, 67056 Ludwigshafen, Germany

A B S T R A C T

We propose a multiregion approach to allow for the computational fluid dynamic simulation of heterogeneous fixed bed reactors with a microkinetic description of the surface reactivity and the concomitant account for intraphase transport. A partitioned approach has been considered for the coupling between the different regions. The computational domain is split in different regions, which are characterized by different phenomena. The governing equations in the different regions of the domain are solved sepa-rately, followed by the achievement of the convergence at the boundaries through an iterative procedure. Overall, the resulting numerical framework allows for the dynamic solution of reacting flows over solid porous catalysts of arbitrary complex geometries with surface reactivity described by detailed microki-netic mechanisms. The capabilities of the numerical framework are tested through the analysis of complex geometries and large heterogeneous microkinetic models and the simulation of experimental data of H_2 combustion on Rh in conditions where internal mass transfer limitations are controlling.

1. Introduction

Catalysts are functional materials or molecules able to provide 'active sites', which allow for a stabilization of the Gibbs free energy of the transition states of the elementary reactions, thus resulting in an enhanced reaction rate. In heterogeneous gas–solid catalytic reactions, such active sites are, by nature, present in a separate solid phase, which is embedded in a gas phase of reacting species. Thus, the reactants in the gas-phase have to reach the active sites and this involves several physical transport processes [1]. A schematic of such processes is reported in Fig. 1.

All these steps occur at a finite rate and thus concentration (and temperature) gradients may arise among the bulk fluid phase conditions and the ones in proximity of the active site. As a consequence, since the physical steps may have a strong impact on the rate of the overall process, the observable reaction rate may differ substantially from the intrinsic reaction rate of the chemical transformation under bulk fluid phase conditions. Such an interplay between chemistry and transport processes determines the macroscopic observed functionality of the catalyst, which is an intrinsic multiscale property of the system. Indeed, it involves phenomena, which are characterized by very different time and length scales [2]. In a previous work [3], we have successfully proposed a

A R T I C L E I N F O

Article history:
Received 6 May 2015
Received in revised form 6 August 2015
Accepted 9 August 2015
Available online 28 August 2015

Keywords:
Operator-splitting
Multi-region
Internal transport
Microkinetic modeling
Chemical reactor
Catalysis

* Corresponding author.
E-mail address: matteo.maestri@polimi.it (M. Maestri).
[1] These authors contributed equally to this work.

© 2015. This manuscript version is made available under the CC-BY-NC-ND 4.0 license http://creativecommons.org/licenses/by-nc-nd/4.0/
Published Journal Article available at: http://dx.doi.org/10.1016/j.cej.2015.08.080

Nomenclature

A	area of catalyst (m^2)
Co	Courant number (–)
$\widehat{C}_P$	mass specific heat at constant pressure $\left(\frac{J}{kg\ K}\right)$
$\widetilde{C}_P$	molar specific heat at constant pressure $\left(\frac{J}{kmol\ K}\right)$
Di	diffusion number (–)
$\widetilde{H}$	molar enthalpy $\frac{J}{kmol}$
NCG	number of gas species (–)
NCS	number of adsorbed species (–)
NR	number of reactions (–)
$\widetilde{S}$	molar entropy $\left(\frac{J}{kmol\ K}\right)$
T	temperature (K)
t	time (s)
v	velocity $\left(\frac{m}{s}\right)$
V	volume of catalyst (m^3)
W	molecular weight $\left(\frac{kg}{kmol}\right)$
x_k	mole fraction of species k (–)

Greek symbols

α_{cat}	effective catalytic area per unit of catalytic volume $\left(\frac{m^2_{cat}}{m^3_{sol}}\right)$
Δ	characteristic dimensions of the fluid and solid interface cells (m)
$\Delta\widetilde{H}_i^{het}$	reaction heat of reaction i $\left(\frac{J}{kmol}\right)$
Γ	mass diffusion coefficient $\left(\frac{m^2}{s}\right)$
ε	solid porosity (–)
η	effectiveness factor (–)
λ	thermal conductivity $\left(\frac{W}{m\ K}\right)$
μ	dynamic viscosity $\frac{kg}{m\ s}$
θ_j	site fraction of adsorbed species j (–)
ρ	density $\left(\frac{kg}{m^3}\right)$
ω_k	mass fraction of species k (–)
σ_{cat}	site density $\left(\frac{kmol}{m^2}\right)$
r_i^{het}	net reaction rate of reaction i due to the heterogeneous reactions $\left(\frac{kmol}{m^2_{cat}\ s}\right)$
$\widetilde{\Omega}_k^{het}$	net formation rate of species k due to the heterogeneous reactions $\left(\frac{kmol}{m^2_{cat}\ s}\right)$

Superscripts

eff	effective property in solid region (–)
G	gaseous phase (in solid or fluid regions) (–)
I	interface between fluid and solid regions (–)
S	solid phase (in solid regions) (–)

Subscripts

fluid	fluid region (–)
solid	solid region (–)

numerical framework based on the operator splitting algorithm in order to efficiently couple the Computational Fluid Dynamics (CFD) simulations with a microkinetic description of the surface reactivity. Such methodology has enabled the simulation of multidimensional systems with complex kinetic mechanisms and turned out to be of great relevance in assisting the analysis and design of catalytic devices for processes where a strong interaction between chemistry and transport occurs [4]. The focus of the methodology was on the coupling between the fluid flow and microkinetic modeling of the surface reactivity. For simplicity porous diffusion was neglected. Nevertheless, in gas–solid heterogeneous reactions, the 'active site' is usually supported or present in a solid with given structure and porosity. Therefore, transport processes are not only associated with the mass transfer from the bulk of the fluid to the surface of the solid catalyst, but also with the diffusion and reaction within the porous solid catalyst. Such phenomenon may give rise to concentration and temperature gradients within the solid, which means that not all the active sites work at the same conditions of reactant chemical potential. Such internal transport limitations can have a strong impact on the observed reaction rate, especially in the presence of long diffusion path lengths or fast (e.g., compared to diffusion) reaction rates. As a consequence, the inclusion of this effect is of crucial importance in order to achieve a quantitative description of the reacting system behavior.

In view of this, here we extend the previously developed numerical framework for the CFD analysis of heterogeneous reactors with a microkinetic description of the surface reactivity to the concomitant account for internal transport. In particular, in order to couple the solution of the transport equations in the fluid phase with the transport phenomena in the solid phase(s), a multi-region model has been considered. The whole computational domain is split in different regions, which are characterized by different phenomena and thus different governing equations. To overcome the complexity of the numerical problem, a segregated approach has been implemented for coupling between the different neighboring regions at the interface, which involves the solution of the different governing equations in each region, followed by the achievement of convergence at the boundaries through an iterative procedure. The resulting numerical framework allows for the dynamic solution of reacting flows over solid porous catalysts. The surface reactivity is described by detailed microkinetic mechanisms with in principle no limits on the number of species

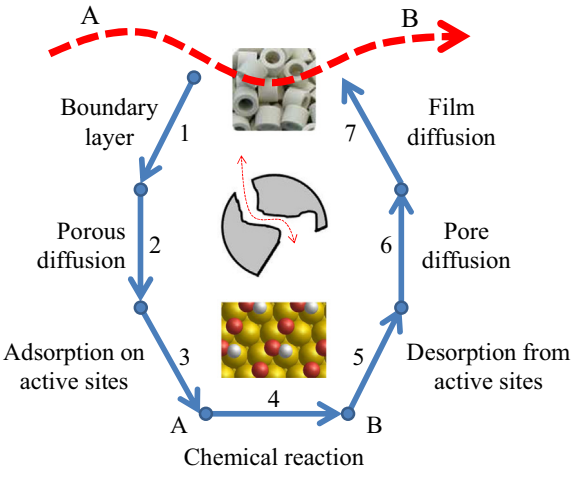

Fig. 1. Main physical and chemical steps involved in the catalytic process. (1) interphase diffusion of the reactants from the bulk to catalyst surface through the boundary layer; (2) intra-phase diffusion of the reactants through the porous structures; (3–5) adsorption, surface reaction, and desorption, respectively; (6) intra-phase counter-diffusion of the products by the porous channels; and (7) intra-phase counter diffusion of the products from catalyst surface to bulk through the boundary layer.

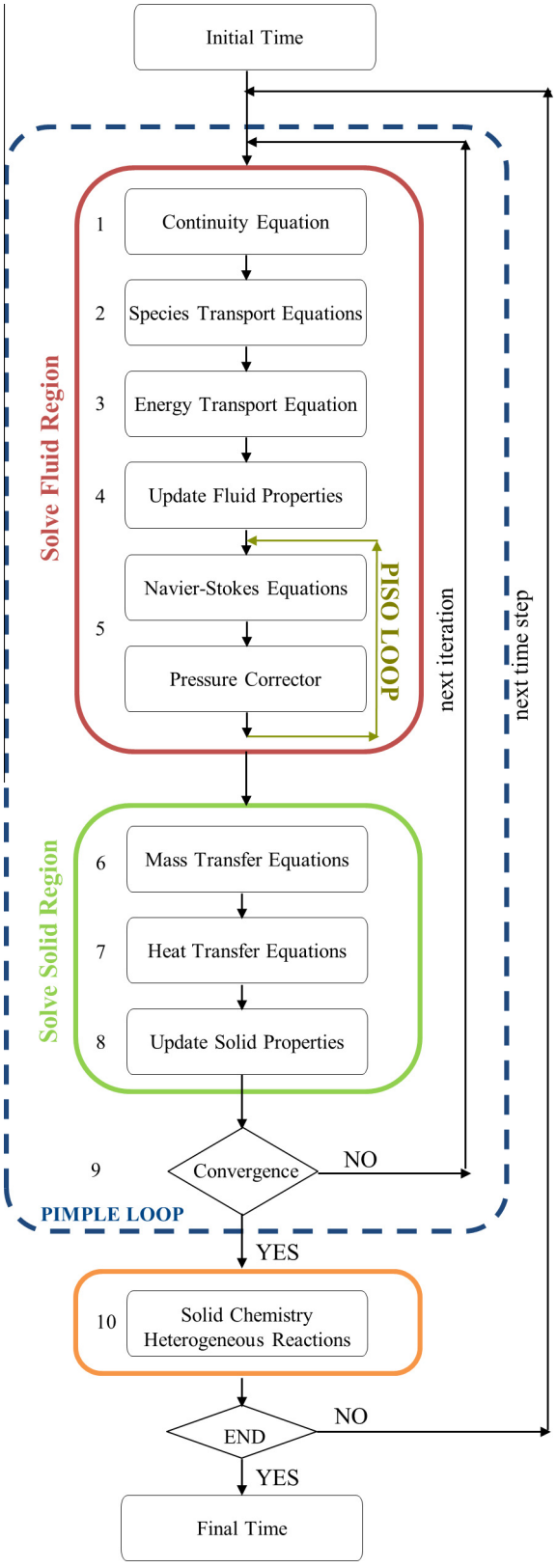

Fig. 2. PIMPLE-chemistry loop algorithm employed in the catalyticFoam-MultiRegion solver.

and reactions and the possibility to investigate systems with geometries of arbitrary complexity. For the description of the diffusion and reaction in the solid regions, we adopt a pseudo-phase approach by employing effective transport coefficients, but the algorithm herein proposed can be extended to different models for diffusion (e.g., dusty-gas model [5]).

The paper is organized as follows. In the first part, the numerical architecture of the solver is presented and tested over selected cases in order to assess reliability and soundness of the methodology. In the second part of the paper, several show-cases are presented. In particular, the analysis of fuel-rich H_2 combustion over Rh experiments, where a strong impact of internal mass transfer limitations were detected, is reported. Then, the capability of the algorithm is tested by the analysis of complex geometries and large heterogeneous microkinetic models.

2. Governing equations

The proposed framework has been developed for the numerical modeling of steady and unsteady-state, multidimensional, and multiphase catalytic systems with arbitrary geometries and detailed microkinetic mechanisms for homogeneous and heterogeneous chemistries. The governing equations, which are solved in each region, are summarized in the following.

2.1. Fluid-region

The reactive flow is described by the mass, energy and momentum conservation equations for continuous, multicomponent, compressible, thermally-perfect mixtures of gases [6]. In particular, the full Navier–Stokes equations are solved for obtaining the (laminar) flow field. A detailed description of these equations is reported in Maestri and Cuoci [3].

2.2. Solid-region

The solid phase, which can in principle consist of different regions, is modeled as a fictitious pseudo-homogeneous phase. This system, which is intrinsically heterogeneous, has been modeled as a pseudo-phase, with isotropic and uniform morphological properties specific for each region.

Thus, the problem can be described as the diffusion and reaction of the fluid in the pseudo-phase. In particular, the conservation equations of individual gaseous species, mixture energy, and adsorbed species are written as shown in the following:

$$\frac{\partial(\rho^G\omega_k)}{\partial t} = \nabla\cdot\left(\rho^G\Gamma_k^{eff}\nabla\omega_k\right) + \alpha_{cat}W_k\widetilde{\Omega}_k^{het} \quad k = 1,\ldots,\mathrm{NCG} \tag{1}$$

$$\left(\rho^S\widehat{C}_P^S(1-\varepsilon) + \rho^G\widehat{C}_P^G\varepsilon\right)\frac{\partial T}{\partial t} = \nabla\cdot\left(\lambda^{eff}\nabla T\right) - \alpha_{cat}\sum_{i=1}^{NR}\Delta\widetilde{H}_i^{het}r_i^{het} \tag{2}$$

$$\sigma_{cat}\frac{d\theta_j}{dt} = \widetilde{\Omega}_j^{het} \quad j = 1,\ldots,\mathrm{NCS} \tag{3}$$

Transport properties in this pseudo-phase are evaluated by means of effective transport coefficients. Such effective transport properties retain all the information regarding the effect of the structure on transport and can be evaluated according to different models [7,8].

The mean-field approximation [9] is applied to evaluate the surface reaction rate. Nevertheless, the algorithm is not restricted to mean-field approximation and can be employed also using kinetic Monte Carlo simulations of the surface reactivity, as we proposed in [10]. Moreover, due to the low gaseous volumes inside the solid pores, homogeneous reactions in the catalyst matrix are neglected.

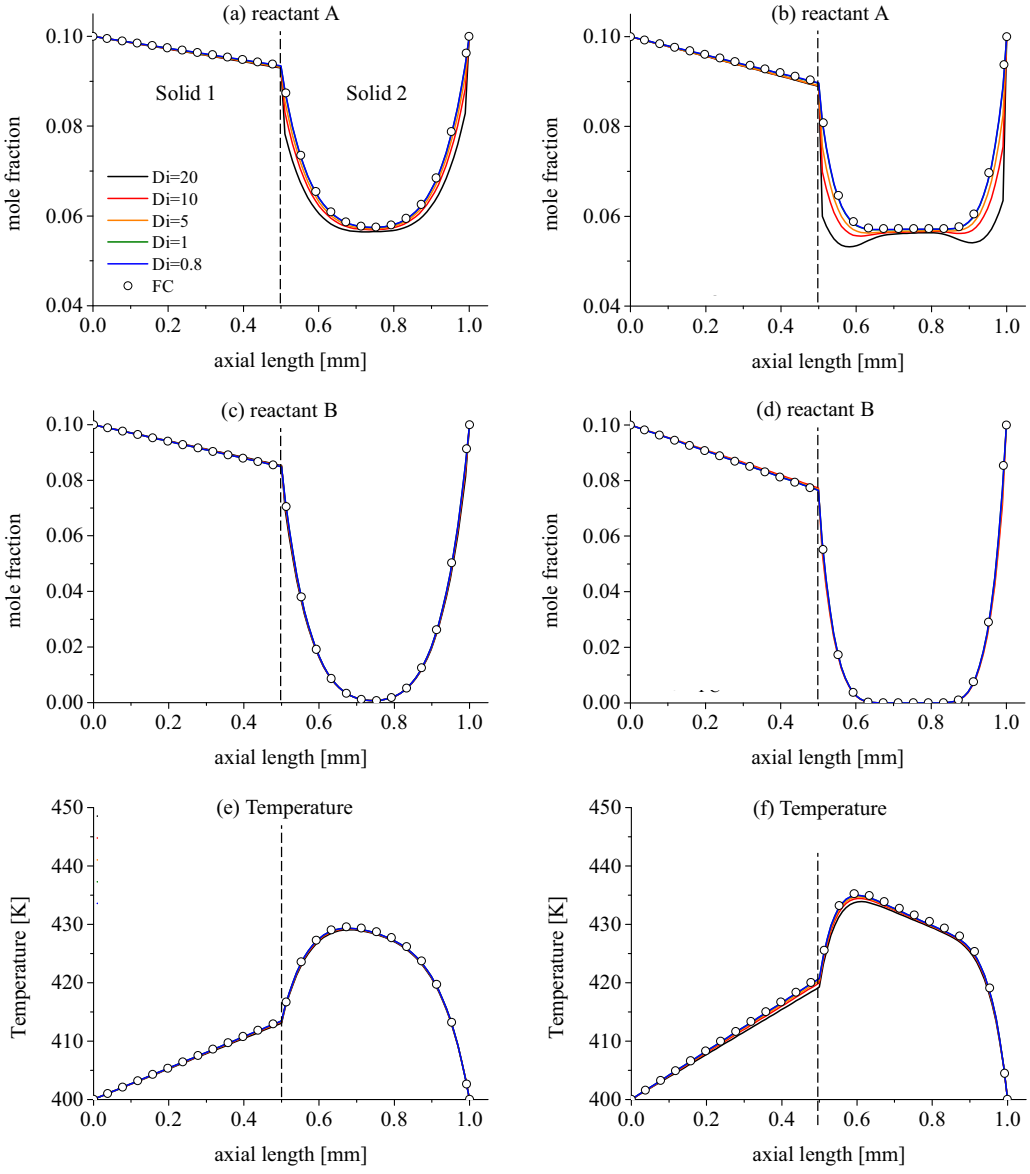

Fig. 3. Monolithic and partitioned algorithms. Comparison between the numerical predictions of the monolithic – fully coupled (FC) algorithm (points) and the partitioned algorithm (lines) at different *Di* numbers in two parallel slabs under different reactivity (α_{cat} in panels a, c, e = 2000 m^2_{cat}/m^3_{solid}, α_{cat} in panels b, d, f = 6000 m^2_{cat}/m^3_{solid}). Panels a–d: mole fraction profiles of reactant species A and reactant B ($\Gamma_{A,solid1} = 2 \times 10^{-4}$ m^2/s, $\Gamma_{B,solid1} = 4 \times 10^{-5}$ m^2/s; diffusivity in solid 2 is 40 times lower that of in solid 1 for all species). Panels e–f: temperature profiles (λ^{eff}_{solid1} = 2.5 W/m/K, λ^{eff}_{solid2} = 0.25 W/m/K). Boundaries conditions: mole fraction *A* = 0.1, mole fraction *B* = 0.1, temperature = 400 K. Only solid 2 is reactive.

2.3. Boundary conditions

In order to solve the conservation equations of total mass, mixture momentum, mixture energy, individual gaseous and adsorbed species in a multiphase system, it is necessary to define proper boundary conditions for the pressure, velocity, temperature, mass and surface site fractions. The boundary conditions for the temperature and mass fractions of the gas species at the inlet and outlet boundaries along with the ones at the inert walls have been already discussed in Maestri and Cuoci [3].

On top of this, the multiregion approach requires the definition of proper boundary conditions at the interfaces between the different regions of the domain, which are characterized by the same value of mass and heat fluxes and by the same value of the species mass fractions and temperature. This leads to the following conditions for mass fraction of *k*-th gaseous species:

$$-\rho_{region,i}\Gamma_{k,eff}\nabla\omega_k\Big|_{region,i} = -\rho_{region,j}\Gamma_{k,eff}\nabla\omega_k\Big|_{region,j} \quad k = 1,\ldots,\mathrm{NCG} \tag{4}$$

$$\omega^I_{k,region,i} = \omega^I_{k,region,j} \quad k = 1,\ldots,\mathrm{NCG} \tag{5}$$

and for temperature:

$$-\lambda_{fluid}\nabla T\big|_{region,i} = -\lambda_{eff}\nabla T\big|_{region,j} \tag{6}$$

$$T^I_{region,i} = T^I_{region,j} \tag{7}$$

For adsorbed species a Neumann ($\nabla(\cdot) = 0$) boundary condition was employed at the interface boundary and at inert wall. In terms of velocity and pressure fields, the solid regions of the domain are modeled as a stationary region within which transport is described

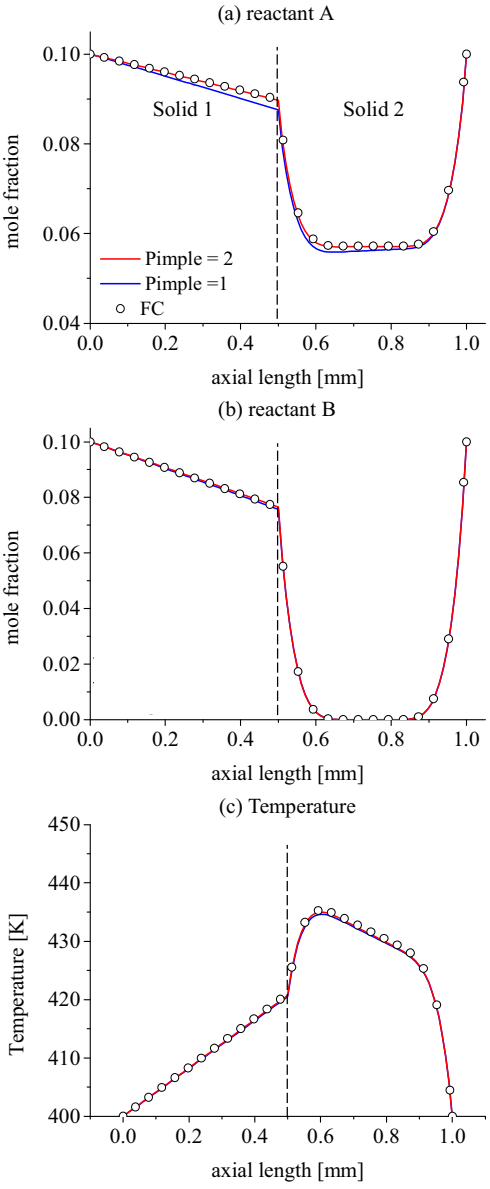

Fig. 4. Effect of the PIMPLE loop. Mole fraction profiles of reactant specie A (a) and reactant B (b) in two parallel slabs with different effective transport properties at different PIMPLE loops. The operating conditions are the same of Fig. 3. Lines refer to the operator splitting algorithm; symbols refer to the monolithic – fully coupled (FC) method.

by diffusion and reaction without convection. Therefore, non-slip and Neumann boundaries conditions were applied to the velocity and pressure fields, respectively, at the gas/solid boundaries.

2.4. Thermodynamic and transport properties of gas phase

The thermodynamic and transport properties of gaseous species and mixtures are calculated using the OpenSMOKE++ framework [11]. The thermodynamic properties of each gaseous species are calculated according to the approach proposed by Gordon and McBride [12]. For each species, the dimensionless thermodynamic properties at constant pressure are specified as functions of temperature as follows:

$$\frac{\widetilde{C}^{G}_{P,k}}{R} = a_{k,1} + a_{k,2}T + a_{k,3}T^2 + a_{k,4}T^3 + a_{k,5}T^4 \tag{8}$$

$$\frac{\widetilde{H}_{k}}{RT} = a_{k,1} + \frac{a_{k,2}}{2}T + \frac{a_{k,3}}{3}T^2 + \frac{a_{k,4}}{4}T^3 + \frac{a_{k,5}}{5}T^4 + \frac{a_{k,6}}{T} \tag{9}$$

$$\frac{\widetilde{S}^{G}_{k}}{R} = a_{k,1}\ln T + a_{k,2}T + \frac{a_{k,3}}{2}T^2 + \frac{a_{k,4}}{3}T^3 + \frac{a_{k,5}}{4}T^4 + a_{k,7} \tag{10}$$

where $\widetilde{C}^{G}_{P,k}$, $\widetilde{H}^{G}_{k}$, and $\widetilde{S}^{G}_{k}$ are the molar specific heat at constant pressure, the molar specific enthalpy and the molar specific entropy (at 1 atm) of species k-th, respectively. T is the temperature, R the universal gas constant, and $a_{k,1} - a_{k,7}$ are the least-squares coefficients of the Gordon and McBride empirical equations [12]. For each species, two sets of coefficients for use on two adjacent temperature intervals are included, resulting on an overall number of parameters equal to 14.

The thermodynamic properties of the gaseous mixture are evaluated by applying the Gibbs theorem, which consists in summing up the contributions made by all species. For example, the mixture molar-specific enthalpy $\widetilde{H}$ is given by $\widetilde{H}^{G} = \sum_{k=1}^{NCG} x_k \widetilde{H}^{G}_{k}$, where x_k is mole fraction of species k-th.

The transport properties of the species are computed by using the standard kinetic theory expressions [13,14]. To expedite the evaluation of transport properties, we fit the temperature dependent parts of the pure species property expressions. This means that, rather than re-evaluating the complex expressions for the properties, only simple fits need to be evaluated. In particular, following the approach used by CHEMKIN® [15], we use a polynomial fit of the logarithm of the property versus the logarithm of the temperature:

$$\ln \mu^{G}_{k} = \sum_{j=1}^{N} b^{\mu}_{k,j} (\ln T)^{j-1} \tag{11}$$

$$\ln \lambda^{G}_{k} = \sum_{j=1}^{N} b^{\lambda}_{k,j} (\ln T)^{j-1} \tag{12}$$

$$\ln \Gamma^{G,0}_{i,k} = \sum_{j=1}^{N} b^{\Gamma}_{i,k,j} (\ln T)^{j-1} \tag{13}$$

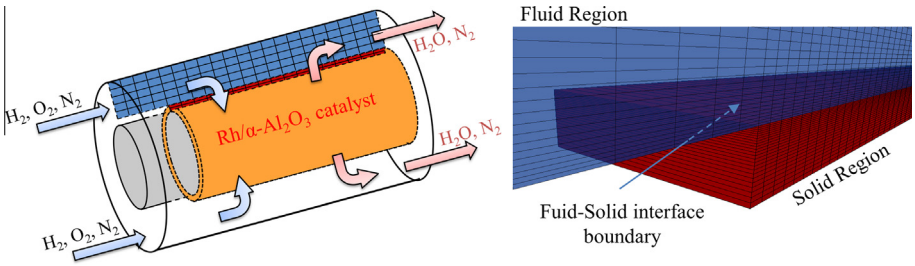

Fig. 5. Sketch of the annular reactor (left) and part of computational domain in correspondence of the beginning of the catalysis layer (right). The first 5 mm of the reactor length are inert.

Table 1
Operating conditions, reactor geometry, and catalyst properties of the H_2 combustion on Rh in annular reactor.

Operating conditions	
H_2 mole fraction	0.04
O_2 mole fraction	0.01
N_2 mole fraction	0.95
Inlet velocity	0.274 Nl/min
Inlet temperature	323–823 K
Reactor geometry	
Inner radius	0.235 cm
Outer radius	0.450 cm
Reactor length	1.5 cm
Catalysis thickness	50 μm
Catalyst properties	
α_{cat}	5×10^4 m^2_{cat}/m^3_{cat}
Porosity	0.55
Tortuosity	8
Radius pore	0.05 μm

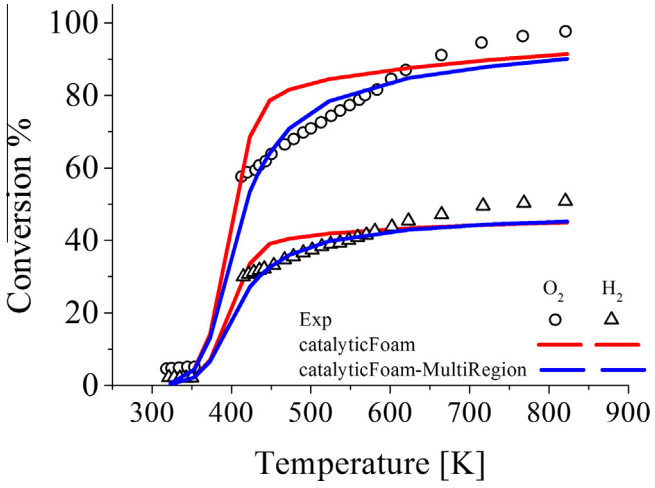

Fig. 6. Annular reactor: conversion of reactant species. Empty circles and triangles refer to experimental conversion of O_2 and H_2, respectively; red lines refer to numerical results of catalyticFoam solver; blue lines refer to numerical results of catalyticFoam-MultiRegion. (For interpretation of the references to color in this figure legend, the reader is referred to the web version of this article.)

where μ_k^G and λ_k^G are the dynamic viscosity and the thermal conductivity of species k-th, respectively. $\Gamma_{i,k}^{G,0}$ is the binary mass diffusion coefficient between species i-th and k-th evaluated at the pressure of 1 bar. The $b_{k,j}^{\eta}$, $b_{k,j}^{\lambda}$, $b_{i,k,j}^{\Gamma}$ coefficients are the fitting parameters for viscosity, thermal conductivity, and mass diffusion, respectively.

Third-order polynomial fits (i.e., $N = 4$) are adopted (as suggested in [15], where it is reported that the average error is well within 1%). Obviously, the fitting procedure has to be carried out for the particular gaseous mixture under investigation, which means that the fitting cannot be done "once and for all," but must be done once at the beginning of each new problem. Moreover, while the viscosities and conductivities of species do not depend on the pressure, the binary diffusion coefficients inversely depend on pressure. The Eq. (13) refers at unit pressure of 1 bar and therefore the real evaluation of a binary diffusion coefficient $\Gamma_{i,k}^G$ at pressure p (in bar) is given by $\Gamma_{i,k}^G = \Gamma_{i,k}^{0,G}/p$.

The mixture diffusion coefficient $\Gamma_{k,mix}^G$ for species k-th is calculated using the following expression [16]:

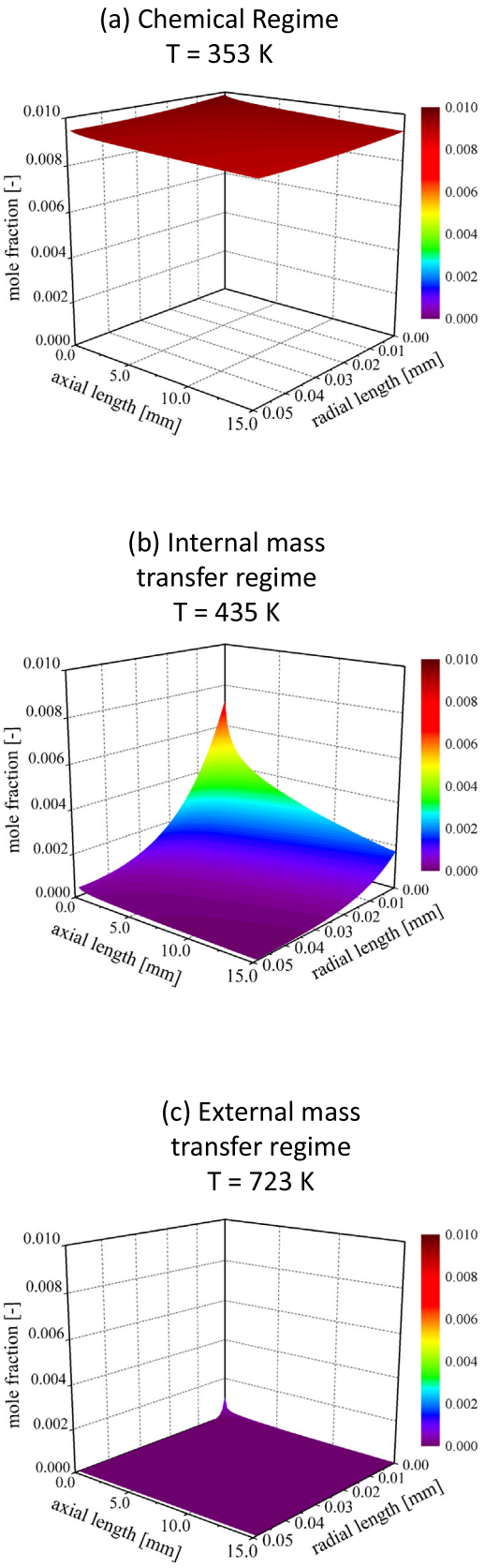

Fig. 7. Annular reactor: maps of O_2 concentration for three different temperatures. (a) Chemical regime (323–373 K); (b) internal mass transfer regime (423–523 K); (c) external mass transfer regime (623–823 K). The interface boundary corresponds to axis at radial coordinate = 0.0 mm.

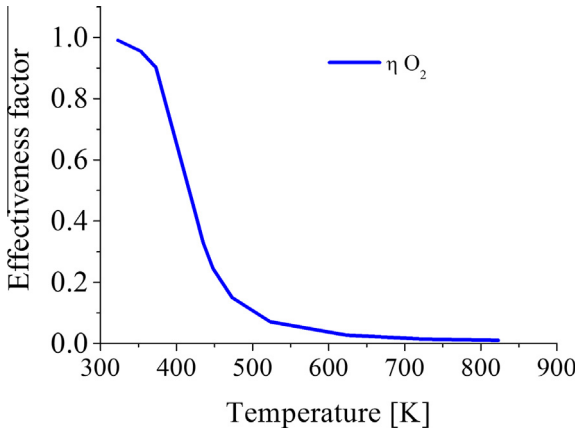

Fig. 8. O_2 effectiveness factor versus temperature in H_2 fuel rich combustion on Rh annular reactor.

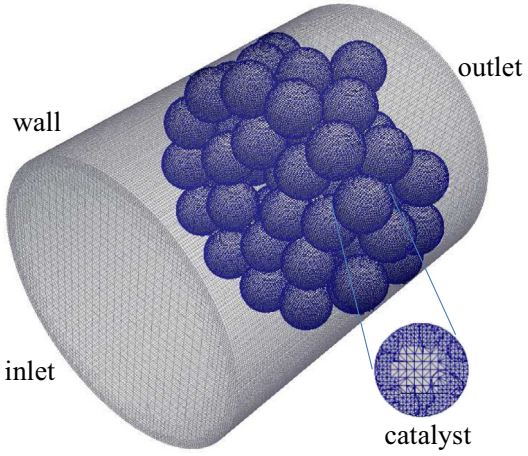

Fig. 9. Packed bed reactor geometry. Length 4 cm, diameter 3.2 cm. Sphere diameter is 0.6 cm.

Table 2
Operating conditions, reactor geometry, and catalyst properties of the H_2 combustion on Rh in packed bed spheres reactor.

Operating conditions	
H_2 mole fraction	0.04
O_2 mole fraction	0.01
N_2 mole fraction	0.95
Inlet velocity	0.2 m/s
Inlet temperature	473 K
Wall temperature	473 K
Reactor geometry	
Reactor diameter	3.2 cm
Reactor length	4.0 cm
Catalysis diameter	0.6 cm
Number of particles	50
Catalyst properties	
α_{cat}	500 m^2_{cat}/m^3_{cat}
Effective diffusivity	0.02 Γ^G
Conductivity	2.5 W/m/K
Porosity	0.55
Density	2300 kg/m^3

$$\Gamma^G_{k,mix} = \frac{\sum_{j\neq k}^{NCG} x_j W_j}{W_{mix} \sum_{j\neq k}^{NCG} \frac{x_j}{\Gamma^G_{j,k}}} \tag{14}$$

The remaining mixture-averaged transport properties are then estimated from the corresponding pure species properties through the application of proper mixing rules. In case of dynamic viscosity, the Wilke formula [17] is accounted for:

$$\mu^G = \sum_{k=1}^{NCG} \frac{x_k \mu^G_k}{\sum_{j=1}^{N_S} x_j \phi_{kj}} \tag{15}$$

where:

$$\phi_{k,j} = \frac{1}{\sqrt{8}} \sqrt{\frac{W_j}{W_k + W_j}} \left[1 + \sqrt{\frac{\mu^G_k}{\mu^G_j}} \left(\frac{W_j}{W_k} \right)^{1/4} \right]^2 \tag{16}$$

and W_k is the molecular weight of species k-th. For the thermal conductivity the combination averaging formula proposed by Mathur et al. [18] is adopted:

$$\lambda^G = \frac{1}{2} \left[\sum_{k=1}^{NCG} x_k \lambda^G_k + \sum_{k=1}^{NCG} \frac{x_k}{\lambda^G_k} \right)^{-1} \tag{17}$$

3. Numerical methodology

The numerical solution of the equations reported in the previous section is a challenging task, especially when multidimensional, multiphase, complex geometry, and detailed kinetic mechanism for heterogeneous reactions are taken into account. In this context, an efficient numerical approach is represented by the operator splitting methods [3,19,20]. In extending the previous catalyticFoam solver [3] to a multi-region architecture, particular attention has to be paid to the coupling between the different regions of the system. When dealing with multiple regions with different properties, both monolithic (fully-coupled) and partitioned approaches have been proposed in the literature [21–25]. Several advantages and drawbacks can be found on both methods. On one hand, in the application of monolithic approaches, the solutions of the equations, the storage of the field variables, and all the post-processing operations, as well as parallel processing handling, become intractable with a single matrix approach [24]. On the other hand, partitioned approaches solve separately each of the coupled regions and requires an iterative procedure to reach the convergence of the variables at the interfaces between the regions [25]. Also, partitioned approaches have been proven to efficiently handle multiple regions even for stiff inter-equation coupling. Given our aim of coupling multiregion CFD approaches with detailed microkinetic modeling in heterogeneous catalysis, partitioned approaches turn out to be the most appropriate algorithm to handle the coupling between fluid and solid regions for the case in point. Thus, we implemented the proposed algorithm in the open-source OpenFOAM® framework [26], by modifying the previously developed catalyticFoam solver [3] to manage the coupling between the different regions of the domain.

The architecture of the new solver is based on the PIMPLE algorithm, which is obtained combining the SIMPLE and PISO algorithms that are commonly used in the simulation of compressible reactive flows. In particular, the SIMPLE method (Semi-Implicit Method for Pressure-Linked Equations) is essentially a guess-and-correct procedure for the calculation of pressure, while the PISO algorithm (Pressure Implicit Splitting of Operators) is an iterative procedure for the pressure–velocity calculation developed as an extension of the SIMPLE method for unsteady compressible flows. The PIMPLE algorithm combines these two methods with the aim to improve the numerical stability of the overall procedure.

Moreover, in this context, the PIMPLE algorithm is used to guarantee the coupling among the interface of different phases through an iterative procedure. The mixed boundaries conditions defined

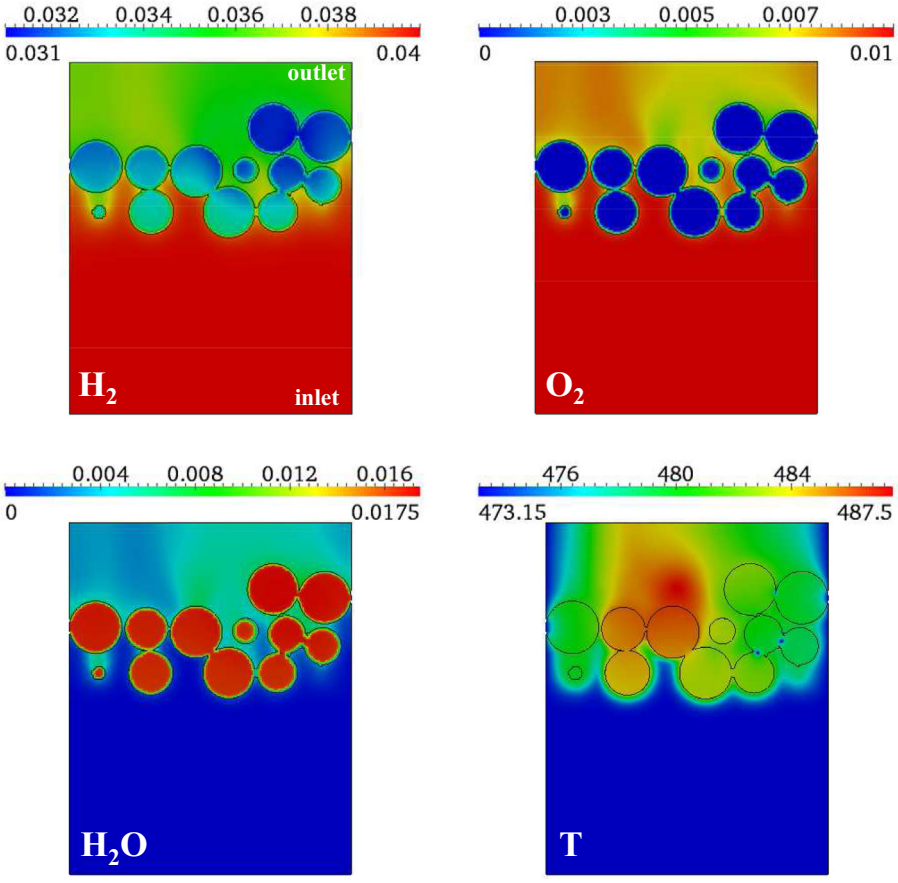

Fig. 10. Packed bed reactor: maps of the main gaseous species (mole fraction) and temperature in the central plane of the computational domain. Inlet from bottoms.

by Eqs. (4)–(7) are solved by deriving a conjugate interface boundary, which has been applied to the mass fraction and to the temperature, as proposed by Dixon et al. [22]. In the following, we will refer to a fluid phase in contact with only one solid phase for the sake of simplicity. Nevertheless, we stress that the algorithm is not limited to the simulation of only two phases (e.g., fluid and solid), but it can be directly applied to account for the presence of several solid phases with different properties, which are treated as different regions with, e.g., different catalyst loading, active sites, transport properties. The iterative procedure of the PIMPLE-chemistry loop encompasses the following steps for a generic i-th iteration:

(1) the fluid phase governing equations of continuity are solved with the own boundaries conditions;
(2) the governing equations of mass transfer in fluid phase are solved with the interface boundaries conditions for species mass fractions evaluated by the Eqs. (4) and (5), on the basis of the values estimated at the previous iteration $(i-1)$-th:

$$\omega_{k,fluid}^{I,(i)} = \frac{\frac{\rho_{fluid}\Gamma_{k,fluid}\omega_{k,fluid}^{(i-1)}}{\Delta_{fluid}} + \frac{\rho_{solid}\Gamma_{k}^{eff}\omega_{k,solid}^{(i-1)}}{\Delta_{solid}}}{\frac{\rho_{fluid}\Gamma_{k,fluid}}{\Delta_{fluid}} + \frac{\rho_{solid}\Gamma_{k}^{eff}}{\Delta_{solid}}} \quad k = 1,\ldots,\mathrm{NCG} \tag{18}$$

where $\omega_{k,fluid}^{I,(i)}$, is the fluid mass fraction of k-th gas species at the gas/solid interface boundary at i-th iterative step. Δ_{fluid} and Δ_{solid} are the characteristics dimensions of the fluid and solid interface cells (along the direction normal to the boundary), respectively. $\omega_{k,fluid}^{(i-1)}$ and $\omega_{k,solid}^{(i-1)}$ are the fluid and solid mass fraction of the k-th gas species of the interface boundaries cells;
(3) the governing equation of heat transfer in fluid phase is solved, with the interface boundary conditions for temperature evaluated through Eqs. (6) and (7), on the basis of the values estimated at the previous $(i-1)$-th iteration:

$$T_{fluid}^{I,(i)} = \frac{\frac{\lambda_{fluid}T_{fluid}^{(i-1)}}{\Delta_{fluid}} + \frac{\lambda^{eff}T_{solid}^{(i-1)}}{\Delta_{solid}}}{\frac{\lambda_{fluid}}{\Delta_{fluid}} + \frac{\lambda^{eff}}{\Delta_{solid}}} \tag{19}$$

where $T_{fluid}^{I,(i)}$ is the fluid temperature at the gas/solid interface boundary at i-th iterative step, and $T_{fluid}^{(i-1)}$ and $T_{solid}^{(i-1)}$ are the fluid and solid temperatures of the interface boundaries cells;
(4) the mixture properties of the fluid phase are updated;
(5) the momentum equation is solved by means of the PISO loop;
(6) the governing equations of mass transfer in the solid phase are solved with the interface boundary conditions for species mass fractions evaluated by the Eqs. (4) and (5) on the basis of the new values of fluid species mass fraction estimated at point 2 and on the basis of the solid species mass fraction estimated at $(i-1)$-th iteration:

$$\omega_{k,solid}^{I,(i)} = \frac{\frac{\rho_{fluid}\Gamma_{k,fluid}\,\omega_{k,fluid}^{(i)}}{\Delta_{fluid}} + \frac{\rho_{solid}\Gamma_{k}^{eff}\omega_{k,solid}^{(i-1)}}{\Delta_{solid}}}{\frac{\rho_{fluid}\Gamma_{k,fluid}}{\Delta_{fluid}} + \frac{\rho_{solid}\Gamma_{k}^{eff}}{\Delta_{solid}}} \quad k = 1,\ldots,\mathrm{NCG} \tag{20}$$

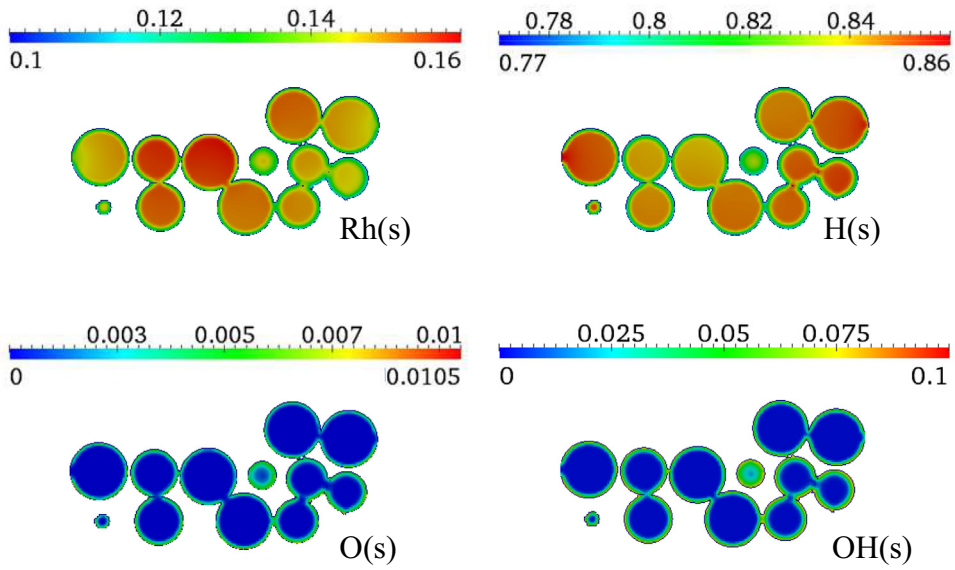

Fig. 11. Packed bed reactor: site fraction maps of the main adsorbed species in the central plane of the computational domain.

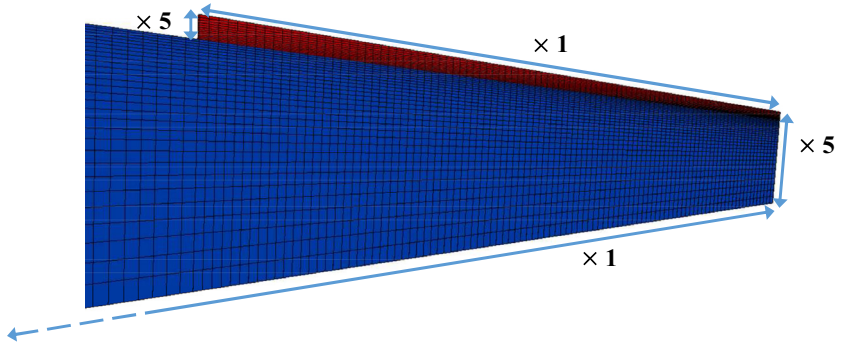

Fig. 12. Computational domain for the circular channel reactor. To better show the solid and fluid mesh, the radial coordinate has been increased by a factor of 5.

Table 3
Operating conditions, reactor geometry, and catalyst properties for isothermal partial oxidation of CH_4 on Rh in a circular channel.

Operating conditions	
CH_4 mole fraction	0.25
O_2 mole fraction	0.14
N_2 mole fraction	0.61
Velocity	0.78
Temperature	1000 K
Reactor geometry	
Reactor diameter	0.1 cm
Reactor length	2.2 cm
Catalysis thickness	50 μm
Catalyst properties	
α_{cat}	$3.8 \times 10^4\ m^2_{cat}/m^3_{cat}$
Porosity	0.5
Effective diffusivity	$0.02\ \Gamma^G$

where $\omega^{I,(i)}_{k,solid}$ is the mass fraction of k-th gas species of solid phase at the gas/solid interface boundary at i-th iterative step;

(7) the governing equation of heat transfer in the solid phase is solved with the interface boundary conditions for temperature evaluated by the Eqs. (6) and (7), on the basis of the new values of temperature of fluid phase estimated at point 3 and on the basis of the solid temperature estimated at $(i-1)$-th iteration:

$$T^{I,(i)}_{solid} = \frac{\frac{\lambda_{fluid} T^{(i)}_{fluid}}{\Delta_{fluid}} + \frac{\lambda^{eff} T^{(i-1)}_{solid}}{\Delta_{solid}}}{\frac{\lambda_{fluid}}{\Delta_{fluid}} + \frac{\lambda^{eff}}{\Delta_{solid}}} \tag{21}$$

where $T^{I,(i)}_{solid}$ is the solid temperature in correspondence to the gas/solid interface boundary at i-th iterative step;

(8) the mixture properties in the solid phase are updated;

(9) convergence checking between the new fluid and solid fields at gas/solid interface boundaries by means of the absolute and relative residuals:

$$\left|\omega^{I,(i)}_{k,fluid} - \omega^{I,(i)}_{k,solid}\right| \leqslant \gamma_J \quad \left|\frac{\omega^{I,(i)}_{k,fluid} - \omega^{I,(i)}_{k,solid}}{\omega^{I,(i)}_{k,fluid}}\right| \leqslant \delta_J \quad k = 1,\ldots,\mathrm{NCG} \tag{22}$$

$$\left|T^{I,(i)}_{fluid} - T^{I,(i)}_{solid}\right| \leqslant \gamma_J \quad \left|\frac{T^{I,(i)}_{fluid} - T^{I,(i)}_{solid}}{T^{I,(i)}_{fluid}}\right| \leqslant \delta_J \tag{23}$$

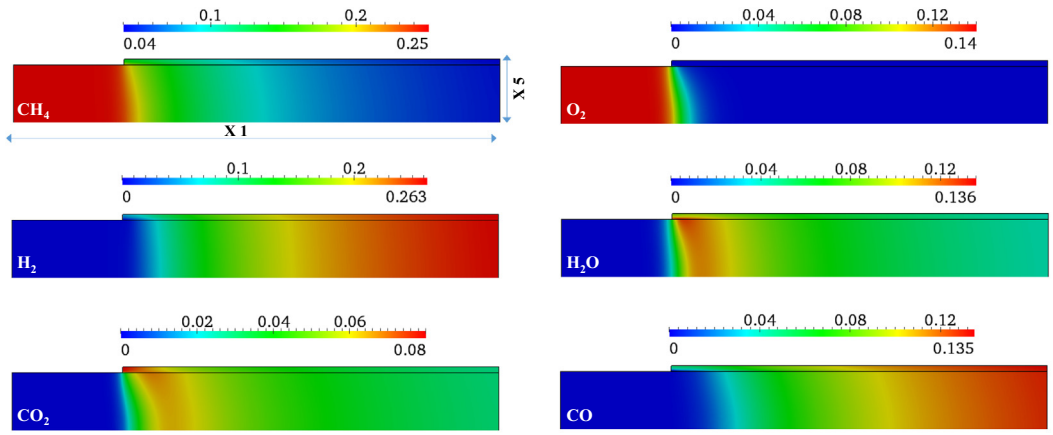

Fig. 13. Mole fraction spatial distribution of the main gas species. The radial coordinate has been multiply by a factor of 5 to better show the overall computational domain.

In this paper, γ_j is set to 10^{-6} and 10^{-5} for the species mass fractions and for the temperature respectively, and δ_j is set to 10^{-3} for both variables.

(10) if convergence is not reached the procedure restarts from point 1;

(11) if the convergence criteria are satisfied, the solver computes the chemistry in the solid phase. Then the solution of the chemistry step is used as starting point for the next time step.

The numerical procedure of PIMPLE-chemistry loop is summarized in Fig. 2. The reactive CFD simulations are carried out with the operator-splitting algorithm implemented in the catalyticFoam solver [3]. Accordingly to the operator splitting [3], the reaction terms are integrated in time using the OpenSMOKE++ ODE solver [11], which is specifically conceived for stiff ODE systems describing reactive conditions.

The selection of the time step is crucial for the successful application of the operator splitting algorithm and has to be performed by considering the different characteristic times of the problem (i.e., convection and diffusion). This is taken into account by considering both the Courant number $Co = \frac{\delta t v}{\Delta}$ (which is defined as the ratio between the time step δt for integration and the time required for the convective transport to cross the smallest cell in the fluid region, i.e. Δ/v), and the diffusion number $Di = \frac{\delta t \Gamma^{eff}}{\Delta^2}$ (which is given by the ratio between time step for integration and the time required for the diffusion transport to cross the smallest cell in the solid region, i.e. Δ^2/Γ^{eff}). To avoid instability problems, both dimensionless numbers have to be lower than unity, and the selection of the integration time is performed considering the smallest time required to fulfill both the conditions. Typically, $Co < 0.1$ and $Di < 0.9$ are sufficiently tight to achieve stability of the solution, as reported in [3] and in Section 4.1 of the present paper, respectively.

4. Results and discussion

In this section we report several applications of the numerical methodology in order to validate the algorithm. First, the validation of the proposed framework by means of a comparison with the monolithic algorithm is proposed. Then, we present the analysis of experimental data of H_2 fuel rich combustion on Rh in an annular reactor, under conditions where internal mass transfer limitations take place. Finally, in order to show the capabilities of the algorithm in dealing with complex geometries and kinetics, the adiabatic combustion of H_2 on Rh in a random packed bed reactor and the isothermal partial oxidation of CH_4 on Rh in monolith channel are reported. All the simulations were performed applying the implicit Euler method and the second order centered scheme for the time and spatial discretization in the transport step, respectively.

4.1. Validation with a fully coupled numerical solutions

To validate the proposed numerical framework, we have considered the comparison between the solutions obtained using the partitioned algorithm and the solution obtained using a monolithic algorithm independently implemented. In the monolithic algorithm, the governing equations of individual gaseous species and mixture energy are solved simultaneously for all the regions, thus representing the most accurate numerical solution. In our case the system has been solved using the finite volume method, imposing the mixed boundaries conditions, defined by the Eqs. (4)–(7), at the interface to couple the different domains of the multi-region system.

In particular, we considered the diffusion and reaction problem in two solid slabs in series, which represent two different regions of the computational domain. Each region (thickness of 0.5 mm and discretization with 50 cells) was characterized by different effective transport properties and by fixed boundaries conditions. The comparison has been performed under adiabatic conditions, employing a single chemical reaction involving two reactants with different effective diffusivities (reactant A has an effective diffusivity higher than reactant B) with an arbitrary non-linear kinetic law $r = k[A][B]^{0.5}$. Fig. 3 shows the comparison between the numerical results according both to the partitioned and the monolithic algorithms, at different values of the Diffusion number. In particular, panels a–d show the comparisons in terms of mole fraction of reactant species, while panels e–f show the comparison in terms of temperature. For $Di > 1$ the solution at steady state differs from the one obtained with the fully coupled algorithm, while for $Di < 0.9$ the solution becomes independent of the choice of the integration time step. In this condition, the predictions corresponding to the two methods are indistinguishable, and, noticeably, the PIMPLE-chemistry loop is able to correctly determine the converged value at the interface both in terms of composition and in terms of temperature for all operating conditions.

Finally, the effect of the number of iterations on the convergence of the PIMPLE loop was investigated. Numerical simulations were performed imposing only one PIMPLE loop at the interface boundary and compared with the ones carried out respecting the criteria of convergence presented above. Fig. 4 shows the effect

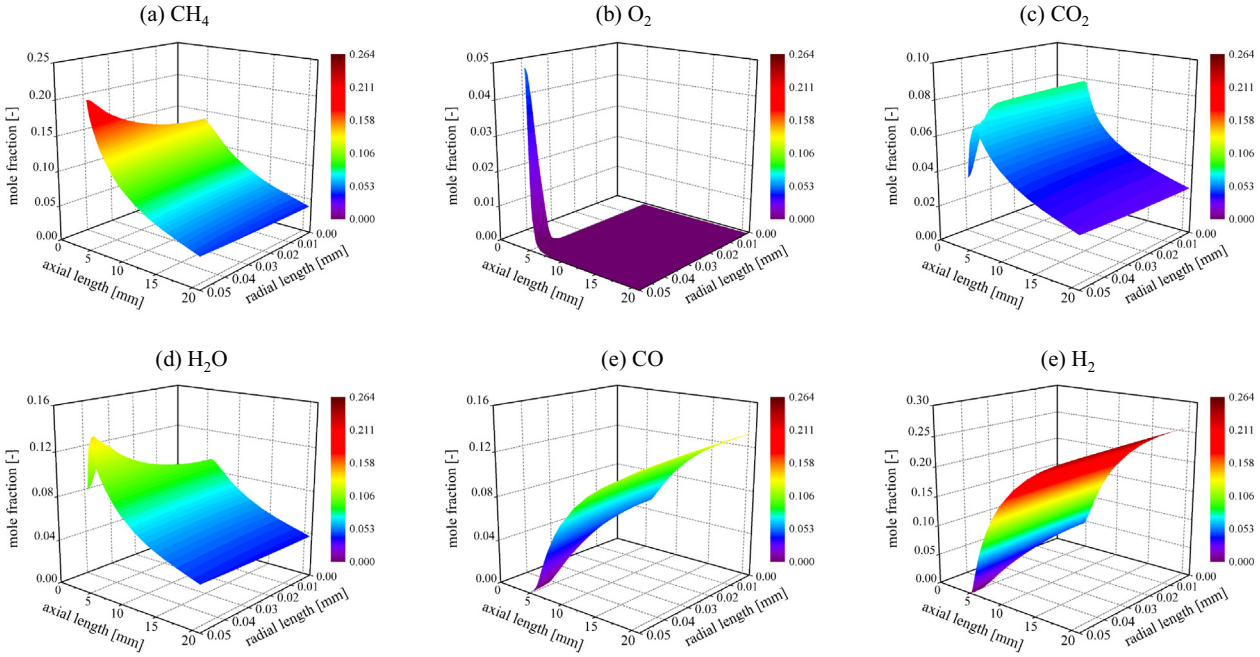

Fig. 14. 3D profiles maps of the main gas species in the solid region. The gas/solid interface boundary corresponds to axis at radial coordinate = 0.05 mm.

of the number of pimple loops which are required to achieve convergence at the interface. Once the convergence is reached, at the second iteration of the PIMPLE loop, the solution obtained with the partitioned algorithm fully agrees with the one obtained with the monolithic algorithm.

After the validation of the algorithm, we now consider three different applications to show the capabilities of the approach.

4.2. H_2 fuel rich combustion on Rh in annular reactor

In this section, we analyze the experimental data of H_2 combustion on Rh in an annular isothermal reactor [27]. The Rh/α-Al_2O_3 catalyst is deposited over the surface of the inner wall reactor forming a uniform and well adherent catalytic layer with a thickness of 50 μm. Due to the cylindrical symmetry of the annular reactor, it was possible to perform simulations over a 2D axial-symmetric domain. Fig. 5 shows part of the computational domain employed in this test, highlighting the fluid and solid regions and the interface boundary. Both regions are refined with a specific grading in correspondence of the strong gradients. Preliminary convergence tests were performed in order to test the stability of the solution with respect to the adopted spatial discretization and the grid independence of the solution. The overall computational domain consists of 2400 solid cells and 8540 fluid cells.

Table 1 reports the operating conditions, the reactor geometric parameters, and the catalyst properties.

The simulations have been carried out employing the detailed UBI-QEP microkinetic model of H_2 combustion [28], which consists of 6 gas species and 5 adsorbed species involved in 18 surface chemical reactions. The parallel pore model was applied to evaluate the effective diffusivity within the catalyst accounting also for Knudsen diffusion [5,16]. The morphological properties of porosity and radius pores, which are needed for the application of the parallel pore model and the evaluation of the Knudsen diffusivity, were experimentally estimated in [27] and reported in Table 1.

Fig. 6 shows the comparison between the numerical results with the experimental data provided in literature [27].

Simulations with and without the account for internal mass transfer limitations are shown. At low temperature ($T < 373$ K), the experimental data show low reactants conversion, followed ($T \sim 425$ K) by a rapid increase in a narrow range of temperature and by a change of the concavity of the curve due to the establishment of the internal diffusion limitation before approaching the external diffusive regime at high temperature ($T > 523$ K). The following main observations can be highlighted:

(1) the multiregion solver shows a satisfactory agreement with the experimental data for both reactants, thus demonstrating the capability of the solver to predict the establishment of all three controlling regimes;
(2) at intermediate temperatures, the simulations performed without taking into account the internal transport phenomena significantly overestimate the experimental data.
(3) At high temperature, where the overall system reactivity is controlled by the external mass transfer, the two models predict same behavior.

For $T > 623$ K the numerical predictions underestimate the experimental data as already explained in Maestri et al. [29]. These trends become apparent when we consider the oxygen profiles in the catalytic washcoat. In particular, Fig. 7 presents the 3D profiles of O_2 mole fraction within the solid phase at three different temperatures.

At low temperature (353 K) there is no O_2 concentration gradient within the catalyst, thus implying that the catalyst is working under chemical regime. At the intermediate temperature (435 K) the O_2 concentration profiles in the catalyst show significant gradient along the radial coordinate due to the establishment of the internal mass transfer limitations. Finally, at high temperature (723 K) the O_2 concentration within the catalysts drops to zero at catalyst interface and the catalysts is working under external mass-transfer regime.

The importance of different regimes can be also expressed in terms of the effectiveness factor:

$$\eta_k = \frac{\frac{1}{V}\int \dot{\Omega}_k^{het} dV}{\frac{1}{A}\int \dot{\Omega}_{k,boundary}^{het} dA} \tag{24}$$

as shown in Fig. 8. For temperatures lower than 373 K, the effectiveness factor for O_2 is close to 1, followed by a sharp decrease as a result of the occurrence of mass transfer limitations.

4.3. Non-isothermal H_2 fuel rich combustion on Rh in a packed bed of spheres

We now consider a more complicated geometry given by a random packed bed of porous spheres. The goal of this analysis is to show the capability and reliability of the solver to handle complex geometries with detailed kinetic mechanisms. The UBI-QEP microkinetic mechanism of H_2 combustion on Rh has been applied in this analysis [28]. Table 2 reports the operating conditions, reactor geometry, and catalyst properties used for the simulation.

Fig. 9 shows the computational domain of the packed bed reactor and details about the geometry. Due to the random sphere distribution inside the reactor, it was not possible to exploit any symmetry of the domain, and thus a 3D simulation was performed. The domain consists of 585,000 fluid domain cells and 275,000 solid domain cells with 130,000 gas/solid interface cells. Bridging among the spheres with a bridge-to-particle diameter ratio of 0.075 is used to properly mesh the contact points between the spheres [30]. Neumann boundary conditions were applied for gas species at the outlet and inert wall boundaries, as well as for the temperature at the outlet boundary. On the contrary, a Dirichlet boundary condition was employed for temperature at inert wall (T_{wall} = 473 K).

The spatial distribution of H_2, O_2, H_2O, and temperature at steady-state is shown in Fig. 10 at a given planar section of the packing. The random packing of the spheres results in a fully not-uniform distribution of reactant and products. Moreover, due to the Dirichlet conditions at the reactor wall, a radial temperature profile establishes in the reactor, as evident from Fig. 10.

Due to the high reactivity and the higher characteristic length of the catalysis sphere, the capability of O_2 to penetrate in the catalyst is quite limited, leading to a low effectiveness factor (η_{O2} = 0.03).

Finally, Fig. 11 shows the spatial distribution of the most abundant surface intermediates (MASI). Due to the higher effective diffusivity and the higher amount of the H_2 than O_2, the H(s) is the MASI of the system in the whole catalyst volume.

The not-uniform distribution of reactant and products results in a concomitant effect on the adsorbed species fields at the boundaries of the packing and within the porous spheres.

4.4. Isothermal partial oxidation of CH_4 on Rh in a circular channel

The analysis has been extended to the isothermal partial oxidation of CH_4 on Rh in a circular channel in order to test the ability of the algorithm in handling more complex microkinetic models. The UBI-QEP microkinetic mechanism of CH_4 combustion on Rh was applied [28]. This kinetic mechanism consists of 15 gas species and 13 adsorbed species involved in 82 surface chemical reactions.

The computational domain, shown in Fig. 12, consists of a circular channel with a diameter of ~1 mm with an external catalyst layer of 50 μm of thickness, placed after 5 mm to fluid inlet. The mesh consists of 5400 cells, with 1200 cells belonging to solid phase. Table 3 reports the operating conditions, geometry, and catalyst properties.

Fig. 13 shows the mole fraction spatial distribution of the main gas species. O_2 is quickly consumed at the beginning of the reactor with immediate formation of H_2O and CO_2, followed by the formation of H_2 and CO by steam reforming reactions.

These trends are also evident in the catalyst washcoat, as shown in Fig. 14. In correspondence of the rapid consumption of O_2 at the reactor inlet (Fig. 14b), a steep O_2 gradient in the washcoat is predicted. As a result, it is possible to observe the rapid formation of CO_2 (Fig. 14c) and H_2O (Fig. 14d), which slowly decrease along the axial and radial coordinate with formation of H_2 and CO. Under the simulated conditions, radial gradients do not seem to arise, except for O_2, without appreciable effects of the internal mass diffusion. Therefore, once O_2 is fully consumed in the gas phase, no evidence of internal mass transport limitations can be observed. This is likely to be due to the small washcoat thickness, which results in high transport rates as compared to the reforming reaction rates.

5. Conclusions

We have proposed a multiregion approach for the CFD simulation of heterogeneous reactors with a microkinetic description of the surface reactivity and concomitant internal mass/energy transport in the porous catalyst. A partitioned algorithm has been used to achieve the convergence of the variables at the interface between fluid and solid. In particular, the PIMPLE algorithm is used for the coupling among the interface of different phases through an iterative procedure that allows to satisfy the mixed boundaries conditions (i.e., continuity of local value and flux). By using as an example the simple case of two neighboring slabs, we have first validated the method through a detailed comparison between the solution obtained with the partitioned and monolithic approaches. The analysis was done by investigating the effect of the different numerical parameters which control the simulation such as number of PIMPLE loops required to achieve convergence at boundary and the selection of time step for the integration. After its validation the framework was then employed for the analysis of experiments of H_2 combustion on Rh with a strong impact of internal mass transfer limitations. Further, simulations of H_2 catalytic combustion in a random packed bed of porous spheres and CH_4 partial oxidation on Rh in monolith channel were also presented to assess and show the capabilities of the proposed numerical framework in dealing with complex geometries and large microkinetic models.

References

[1] O. Deutschmann (Ed.), Modeling and Simulation of Heterogeneous Catalytic Reactions, Wiley-VCH, 2011.
[2] M.P. Dudukovic, Frontiers in reactor engineering, Science 325 (2009) 698–701.
[3] M. Maestri, A. Cuoci, Coupling CFD with detailed microkinetic modeling in heterogeneous catalysis, Chem. Eng. Sci. 96 (2013) 106–117. <www.catalyticfoam.polimi.it>.
[4] T. Maffei, S. Rebughini, G. Gentile, S. Lipp, A. Cuoci, M. Maestri, CFD analysis of the channel shape effect in monolith catalysts for the CH_4 partial oxidation on Rh, Chem. Ing. Tech. 86 (2014) 1099–1106.
[5] G.F. Froment, K.B. Bischoff, Chemical Reactor Analysis and Design, Wiley, New York, 1979.
[6] M.R.J. Charest, C.P.T. Groth, O.L. Gulder, A computational framework for predicting laminar reactive flows with soot formation, Combust. Theor. Model. 14 (2010) 793–825.
[7] A. Wheeler, Catalysis, P.H. Emmett Editor, Reinhold Publishing Corporation, New York, 1955.
[8] N. Wakao, J. Smith, Diffusion in catalyst pellets, Chem. Eng. Sci. 17 (1962) 825–834.
[9] A.B. Mhadeshwar, D.G. Vlachos, Hierarchical multiscale mechanism development for methane partial oxidation and reforming and for thermal decomposition of oxygenates on Rh, J. Phys. Chem. B 109 (2005) 16819–16835.
[10] S. Matera, M. Maestri, A. Cuoci, K. Reuter, Predictive-quality surface reaction chemistry in real reactor models: integrating first-principles kinetic Monte Carlo simulations into computational fluid dynamics, ACS Catal. 4 (2014) 4081–4092.
[11] A. Cuoci, A. Frassoldati, T. Faravelli, E. Ranzi, OpenSMOKE++: an object-oriented framework for the numerical modeling of reactive systems with detailed kinetic mechanisms, Comput. Phys. Commun. 192 (2015) 237–264.
[12] S. Gordon, B.J. McBride, Computer program for calculation of complex chemical equilibrium compositions, rocket performance, incident and reflected shocks, and Chapman-Jouguet detonations (1971).
[13] C.F. Curtiss, J.O. Hirschfelder, Transport properties of multicomponent gas mixtures, J. Chem. Phys. 17 (1949) 550–555.

[14] J.O. Hirschfelder, C.F. Curtiss, R.B. Bird, M.G. Mayer, Molecular Theory of Gases and Liquids, Wiley, New York, 1954.
[15] R.J. Kee, F.M. Rupley, E. Meeks, J.A. Miller, CHEMKIN-III: A Fortran Chemical Kinetics Package for the Analysis of Gas Phase Chemical and Plasma Kineticsm Sandia National Laboratories Report (1996).
[16] R.B. Bird, W.E. Stewart, E.N. Lightfoot, Transport Phenomena, Madison, USA, 1960.
[17] C. Wilke, A viscosity equation for gas mixtures, J. Chem. Phys. 18 (1950) 517–519.
[18] S. Mathur, P. Tondon, S. Saxena, Thermal conductivity of binary, ternary and quaternary mixtures of rare gases, Mol. Phys. 12 (1967) 569–579.
[19] R.J. Kee, J.A. Miller, A split-operator, finite-difference solution for axisymmetric laminar-jet diffusion flames, AAIAA J. 16 (1978) 169–176.
[20] E.S. Oran, J.P. Boris, Numerical Simulation of Reactive Flows, C.U.P. Cambridge (Ed.), 2001.
[21] A.G. Dixon, M. Ertan Taskin, E. Hugh Stitt, M. Nijemeisland, 3D CFD simulations of steam reforming with resolved intraparticle reaction and gradients, Chem. Eng. Sci. 62 (2007) 4963–4966.
[22] A.G. Dixon, M.E. Taskin, M. Nijemeisland, E.H. Stitt, CFD method to couple three-dimensional transport and reaction inside catalyst particles to the fixed bed flow field, Ind. Eng. Chem. Res. 49 (2010) 9012–9025.
[23] S.T. Kolaczkowski, R. Chao, S. Awdry, A. Smith, Application of a CFD code (FLUENT) to formulate models of catalytic gas phase reactions in porous catalyst pellets, Chem. Eng. Res. Des. 85 (2007) 1539–1552.
[24] I. Clifford, Block-Coupled Simulations Using OpenFOAM, 6th OpenFOAM® Workshop, 2011.
[25] B.A. Craven, L.R. Campbell, MRconjugateHeatFoam: A Dirichelet-Neumann Partiotioned Multiregion Conjugate Heat Transfer Solver, 6th OpenFOAM Workshop, 2011.
[26] OpenFOAM, 2013 <www.openfoam.org>.
[27] I. Tavazzi, A. Beretta, G. Groppi, P. Forzatti, Development of a molecular kinetic scheme for methane partial oxidation over a Rh/alpha-Al_2O_3 catalysis, J. Catal. 241 (2006) 1–13.
[28] M. Maestri, D.G. Vlachos, A. Beretta, G. Groppi, E. Tronconi, A C 1 microkinetic model for methane conversion to syngas on Rh/Al 20 3, AIChE J. 55 (2009) 993–1008.
[29] M. Maestri, A. Beretta, T. Faravelli, G. Groppi, E. Tronconi, D.G. Vlachos, Two-dimensional detailed modeling of fuel-rich H_2 combustion over Rh/Al_2O_3 catalyst, Chem. Eng. Sci. 63 (2008) 2657–2669.
[30] A.G. Dixon, M. Nijemeisland, E.H. Stitt, Systematic mesh development for 3D CFD simulation of fixed beds: contact points study, Comput. Chem. Eng. 48 (2013) 135–153.